Rapid Communications

Sonic valley-Chern insulators

Penglin Gao,[1,*] Zhiwang Zhang,[1,2] and Johan Christensen[1,†]
[1]Department of Physics, Universidad Carlos III de Madrid, ES-28916 Leganès, Madrid, Spain
[2]Department of Physics, MOE Key Laboratory of Modern Acoustics, Collaborative Innovation Center of Advanced Microstructures, Nanjing University, Nanjing 210093, China

(Received 13 October 2019; published 2 January 2020)

Topological phases of matter, sound, light, and vibrations have enabled brand new routes to direct and control signals at high fidelity. Chern insulators are known for outcompeting other reciprocal systems in terms of their robustness against crystal imperfections and defects. For sound waves we present the combination of a Chern insulator and a valley-Hall-based configuration and explore novel valley-Chern phases that enable both nonreciprocal band inversion processes and bandwidth broadening of valley-polarized one-way interface states. Interestingly, we find that a valley-Chern system made of two adjacent insulators of which one only breaks the time-reversal symmetry, enables entirely robust waveguiding appearing quantitatively equivalent to the classical Chern insulator. Beyond the rich physics presented, we foresee that our findings may stimulate new research in terms of acoustic waveguiding and control.

DOI: 10.1103/PhysRevB.101.020301

Recent progress in studies on exotic topological phases of matter not only revolutionized our understanding of wave physics but also offers fascinating solutions to manipulate sound, vibrations, and light in unprecedented ways [1–3]. A host of different two-dimensional implementations have already seen the light of day and are categorized as quantum Hall (QH) [4–11], quantum spin-Hall (QSH) [12–20], and quantum valley-Hall (QVH) topological insulators [21–29]. Also, Majorana-like phononic implementations have recently been demonstrated [30,31].

For sound waves, circulating fluid flow was exploited to mimic a synthetic gauge magnetic field responsible to break the time-reversal symmetry (TS) and inducing the QH effect in acoustic Chern lattices [6–9]. Recently, this theoretical proposal has been experimentally demonstrated using hexagonal networks of ring resonators containing rotating fans [32]. In addition, the valley degrees of freedom were found to be an alternative approach to realize topologically protected sound transport brought forward through inversion symmetry (IS) breaking in C_{3v} phononic crystals [23,33]. The topological transition of QH and QVH insulating phases essentially originates from the degeneracy lifting of the Dirac point induced by some particular symmetry breaking mechanisms [34,35]. On this basis, it is possible to gather Chern and valley physics in one unified model when both TS and IS breaking mechanisms are introduced.

In this Rapid Communication, we design an acoustic valley-Chern insulator in a hexagonal waveguide network. Beyond marrying these two subdomains of the classical topological insulator family, we conduct numerical simulations to demonstrate nonreciprocal sound transport both in the structure bulk and along the edges, inherent to the valley-polarized asymmetric one-way band structures. Furthermore, we conduct a quantitative and comparative robustness study among Chern and valley insulators in addition to the combined valley-Chern insulators in order to determine their resilience to bends, cavities, and disorder in an otherwise physically identical environment. In detail, the aforementioned hexagonal waveguide network comprises two coupled ring resonators within the unit cell. The two resonators are dimerized with unequal radii to break the IS while a uniform circulating flow is applied in each resonator to prevent TS. Thus our unified platform is able to embrace both QH- and QVH-based topological systems to unravel novel nonreciprocal and topologically robust sound physics that is readily tuned via geometry and flow.

In Fig. 1(a) we illustrate a man-made lattice containing two distinct ring resonators ("atom" A and B) in the unit cell. Each resonator is interconnected to the nearest neighbors at distance d through straight waveguides, forming a hexagonal network with period $a = \sqrt{3}d$. Indeed, the two ring resonators constitute flexible reconfigurable units to generate the QVH effect merely by varying their geometrical parameters. Here, we introduce the IS breaking mechanism by changing the inner radii $R_{\text{in}}^{\pm} = R_{\text{in}} \pm \delta R$ of the resonators while keeping the outer radii R_{out} unchanged. In a second step, following recent experimental implementations [32], we break the TS by invoking uniformly moving airflow of speed v_0, as indicated by the green vortex arrows [see Fig. 1(a)]. The symmetry intact hexagonal lattice sustains a linearly crossing Dirac-like dispersion relation at the corners of the Brillouin zone based on unbroken TS ($v_0 = 0$) and IS ($\delta R = 0$). On the contrary, the two types of symmetry breaking mechanisms will lift the degeneracies at K or K' and competing valley and Chern effects can be harvested. This combined system can be readily described by an effective massive Hamiltonian [34]

$$H = \nu_D \tau \delta k_x \boldsymbol{\sigma}_x + \nu_D \delta k_y \boldsymbol{\sigma}_y + (m_I + \tau m_T)\boldsymbol{\sigma}_z, \qquad (1)$$

*Corresponding author: gplhit@gmail.com
†Corresponding author: johan.christensen@uc3m.es

 ©2020 American Physical Society

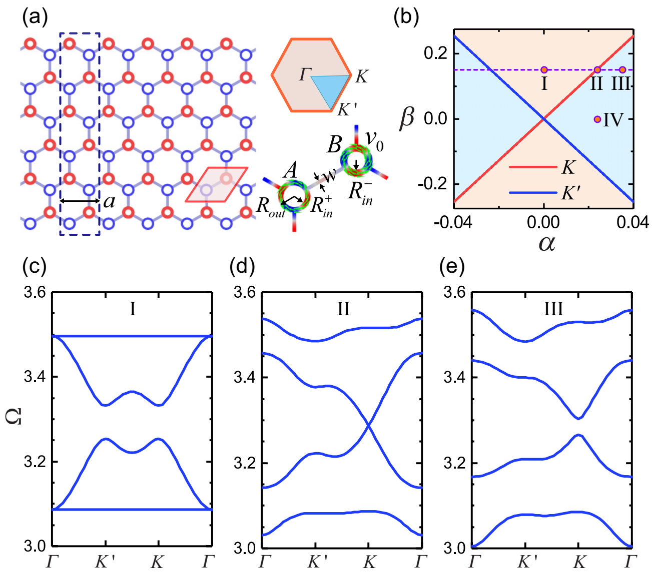

FIG. 1. (a) Schematic of the man-made hexagonal waveguide lattice and the highlighted primitive cell. The two ring resonators A and B are dimerized with unequal inner radii $R_{\rm in}^{\pm}$, each hosting circulating fluid flow (green arrows) to break the TS. (b) The topological phase diagram is plotted against the TS (α) and IS (β) breaking strengths where the red (blue) lines indicate phase boundaries at which the Chern and valley effects are counterbalanced at valley K (K'). The TS breaking strengths are chosen as $\alpha_{\rm I}=0$, $\alpha_{\rm II/IV}=0.024$, and $\alpha_{\rm III}=0.035$. (c)–(e) Bulk dispersion relation of various phases according to the points labeled in the phase diagram in (b). The frequency ω is normalized to $\Omega=\omega a/2\pi c$, with c being the sound speed and a the lattice period.

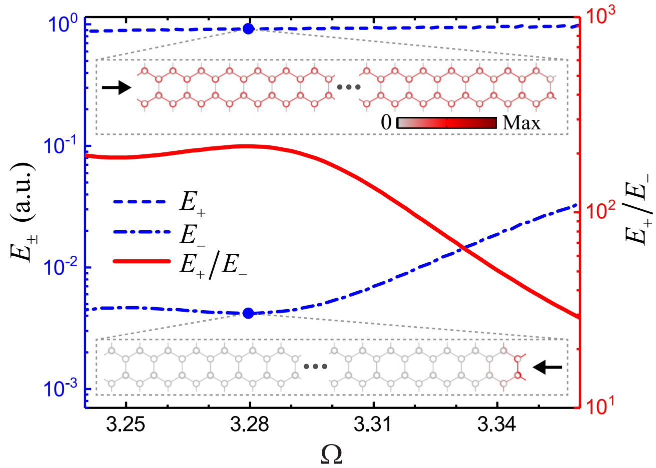

FIG. 2. Calculated time-averaged energy fluxes $E_\pm$ spectra for waves propagating along a ribbon in the forward (+) and backward (−) directions, together with the contrast ratio $\gamma=E_+/E_-$ measuring the nonreciprocity. The insets depict the spatial profiles of the acoustic intensity fields when excited at $\Omega=3.28$ (blue solid dots).

where v_D is the Dirac velocity, $\boldsymbol{\sigma}_i$ are the Pauli matrices, $(\delta k_x,\delta k_y)$ is the wave vector measured at corners K or K', $\tau=\pm1$ denotes the valley degrees of freedom, and m_I and m_T are the mass terms introduced through IS and TS breaking, respectively. Equation (1) illustrates how nonreciprocity comes into effect in a valley-Chern insulator. For one, at one valley both mass terms m_I and m_T are capable to act collectively to a partial band-gap broadening while at the opposite valley, both mechanisms counteract each other, ultimately able to keep the degeneracy intact with zero additional mass, $m_I+\tau m_T=0$. This process is best explained by a topological phase transition process where we plot the valley bands (at K or K') by tuning the two symmetry breaking parameters $\alpha=v_0/c$ and $\beta=\delta R/(R_{\rm out}-R_{\rm in})$. Figure 1(b) illustrates the phase transitions across the intact Dirac cones for the unperturbed scenario $(\alpha,\beta)=(0,0)$. The simulations were implemented using the finite element solver COMSOL MULTIPHYSICS with specific parameters: $R_{\rm in}=0.08a$, $R_{\rm out}=0.13a$, and $w=0.03a$. A linear relationship between α and β is predicted at the phase boundaries, separating four regions hosting either QH or QVH effects. Concretely, when $|m_T|>|m_I|$ the system becomes a Chern insulator while on the contrary, when $|m_T|<|m_I|$, it enters the phase of a valley insulator instead. For example, Figs. 1(c)–1(e) depict the band structures of lattices tuned at various topological phases with constant IS breaking strength $\beta=0.15$ [see dashed line in Fig. 1(b)]. The previous discussion related to the massive Hamiltonian is here clearly manifested in that an increase in the TS breaking strength α induces a transition from a pure reciprocal VH insulator [Fig. 1(c)] to a one-way valley-Chern insulator. As the figures display, at the K' valley we see a steady broadening of the gap, whereas at the K point, the valley undergoes a topological band inversion with growing α. The latter effect is a highly unusual mechanism in that the TS breaking strength controls the closing and the reopening of the topological band gap, which is in stark contrast to the acoustic counterpart of the Zeeman splitting [6,32].

The critical zone of phase II is of particular interest because of the remarkable valley-polarized one-way gapless Dirac spectrum [see Fig. 1(d)] that can enable diodelike sound propagation in the bulk. In order to test it, we numerically construct a finite ribbon across which sound is set to propagate in either forward (K) or backward (K') directions as depicted in the insets of Fig. 2. Computationally, we set the boundary at which the ribbon extends to infinite to periodic, then we are able to compute the time-averaged energy flux $E_\pm$ flowing both outwardly (+) and backwards (−) across the ribbon. The computed spectra of $E_\pm$ together with their contrast ratio $\gamma=E_+/E_-$ is shown in Fig. 2. The mass equilibrium $m_I=-\tau m_T$ ensures an intact Dirac cone that sustains complete sound transport in the forward direction. However, in reverse, due to the gap broadening at the K' valley, the sound wave rapidly decays exponentially into the bulk as the intensity plots depict in the lower inset of Fig. 2, which is characterized by a remarkable contrast ratio of $\gamma>200$ at $\Omega=3.28$ (blue solid dots). We emphasize that this approach is based on a fully linear description leading to novel sound transport via one-way Dirac cones.

We now intend to unravel the characteristics of topological edge states in valley-Chern insulators in dependence to their phases. We begin by calculating the projected band structures for a ribbon with zigzag termination tuned at the aforementioned three distinct topological phases [see Figs. 3(a)–3(c)]. Note, the nonzero breaking pair (α,β) induces not only

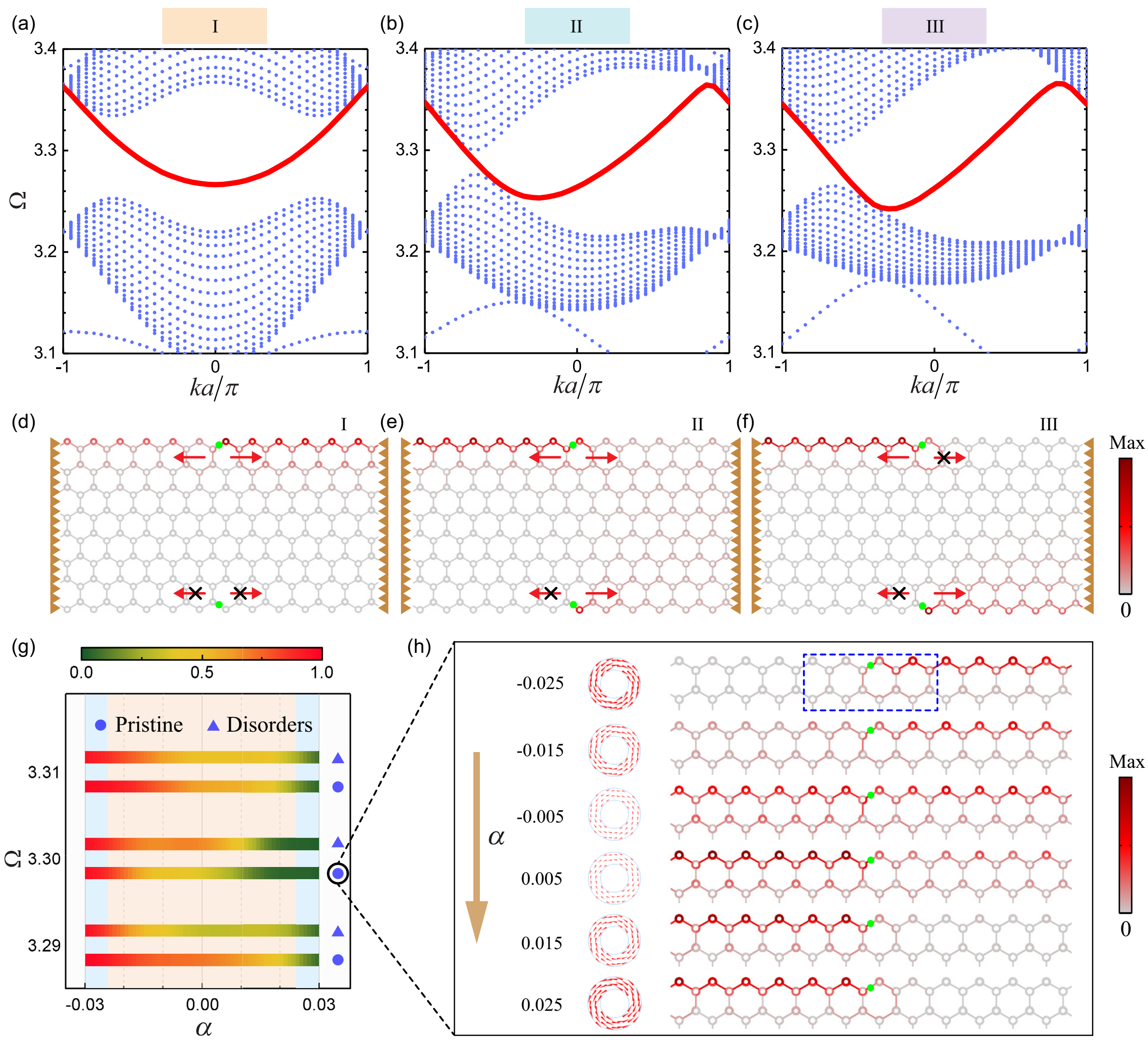

FIG. 3. (a)–(c) Projected bulk dispersion relation for ribbons with zigzag edges and their in-gap edge states as highlighted in red across various valley-Chern phases corresponding to the respective labels in Fig. 1(b). (d)–(f) Intensity fields in response to two monopole sources (green dots, $\Omega = 3.29$). Nonreflecting interfaces are added to the lateral sides to avoid acoustic scattering. (g) Pristine and disordered spectra of the normalized forward energy flux $E_+/(E_+ + E_-)$ against the TS breaking strength α. The background color indicates the topological phase transition similar as in Fig. 1(b). (h) A group of intensity field maps depict the tunability of the nonreciprocal edge states along the upper interface at $\Omega = 3.30$ for various values of α. The corresponding vortices within the ring resonators are plotted to the left of the panel.

asymmetric band gaps as we learned earlier, but gives rise to asymmetric in-gap edge states at the two valleys as well. It is worth mentioning that such states are not always entirely topologically protected, particularly when the system enters the valley regions ($|m_I| > |m_T|$) where the Chern number vanishes. To elucidate both one-way and two-way transport of edge states in these valley-Chern insulators, we implement full wave simulations of a finite lattice made of 12×8 unit cells. A pair of monopole sources (green dots) are placed in the middle of the upper and the lower ribbon terminations to launch forward and/or backward propagating modes along their respective interfaces. With references to the said topological valley-Chern phases, I–III, Figs. 3(d)–3(f) illustrate the spatial profile of the acoustic intensity field at $\Omega = 3.29$, which is near the one-way Dirac point. The pure valley insulator (phase I), sustains two unequal counterpropagating states confined to the upper interface only. Augmenting α towards the critical second phase enables curious wave properties in that insulation characteristics are maintained with a backwards propagating edge state, whereas the opposing mode transports outgoing sound within the entire bulk. Finally, phase III, after relifting the degeneracy of the K valley, clearly displays Chern-typical behavior comprising nontrivial one-way edge states. Figures 3(d)–3(f) hint at the nonreciprocal feature of edge states, i.e., increasing the TS breaking strength enables sound along the top edge from two-way to one-way propagation. Additionally, using the valley-Chern insulator system (point source placed at the top this time) we examine the topological robustness against random defects [introduced within the dashed box in Fig. 3(h)] across various

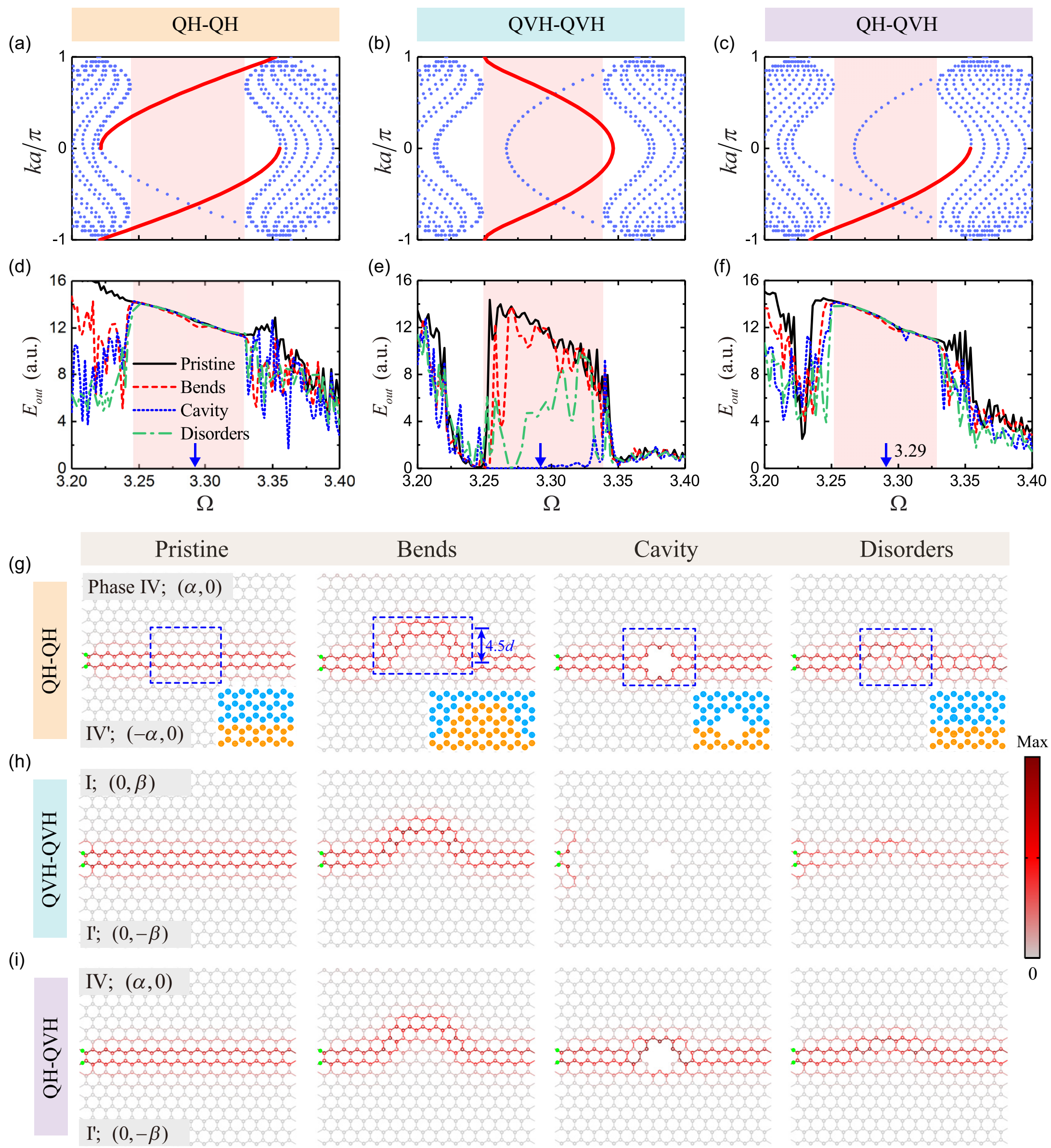

FIG. 4. (a)–(c) Projected bulk band structures for various interface states (depicted in red) supporting insulators, QH-QH, QVH-QVH, and QH-QVH. (d)–(f) The outgoing energy flux $E_{\rm out}$ is spectrally computed for the said topological insulators with typical defects and obstacles as indicated on the inset. (g)–(i) The corresponding spatial intensity maps illustrate how the edge states behave in the presence of these lattice perturbations. In all scenarios, the systems are excited by two monopole sources (green dots, $\Omega = 3.29$).

topological phases. In conducting this study, we compute the normalized forward energy flux $E_+/(E_+ + E_-)$, for several discrete frequencies against α as displayed in Fig. 3(g). Dependent on the handedness of the vortex as determined by the sign of α, the Chern insulating regions, i.e., $|\alpha| > 0.024$, dictate the nonreciprocal edge state strictly to flow along a one-way path irrespective of the perturbations introduced as can be seen in Fig. 3(g). The perturbations are introduced by randomly altering a finite number of the resonator's outer radii $R_{\rm out}^{\pm}$ from a normal distribution (standard deviation $\sigma = 0.01R_{\rm out}$). Deeply within the nonreciprocal Chern phases we predict a complete resilience against those defects, unlike within the valley and valley-Chern phases ($|\alpha| < 0.024$) where intervalley scattering strongly affects the energy flux in the presence of crystal imperfection. In Fig. 3(h), for the pristine hexagonal insulator, the intensity field maps clearly indicate the transition and breakup of sound reciprocity across the various topological valley-Chern phases. In other words, the valley-Chern insulator when tuned by the TS breaking strength constitutes a tunable acoustic diode with threshold at $|\alpha| > 0.024$.

Given the broken TS, it is widely accepted, however without distinctive evidence, that a Chern insulator is less prone to imperfections, therefore, entirely topologically robust, as opposed to a QVH insulator. The bulk-boundary correspondence ensures the existence of robust interface states propagating between insulators of different topological phases. Based on our hexagonal waveguide network, we are capable to construct an equal and fair battleground in which we quantitatively compare Chern (QH-QH) and valley (QVH-QVH) insulators with the same lattice structure leading to spectrally identical band gaps as can be seen in Figs. 4(a) and 4(b). Moreover, with the desire to relax the demands of pure Chern insulators, we intend to reduce the number of resonators that are subject to circulating flow; we further construct a QH-QVH interface to study the advantages of such insulator. In all systems that are illustrated in Figs. 4(g)–4(i) we join the insulators at their zigzag interfaces and unveil their robustness again lattice-scale defects. Using a ribbon supercell as before, we compute the projected band structures of the three hexagonal insulator lattices. The topological interface states are highlighted by red lines in Figs. 4(a)–4(c), while those propagating along the upper and lower free edges are of no interest here and are discarded. Note that the three band diagrams display nearly identical band gaps (shaded background) permitting us to conduct a well-founded comparative study. With reference to the phase diagram in Fig. 1(b), we design the Chern insulator $(\pm\alpha_{\mathrm{IV}}, 0)$ which gives rise to two gapless interface states within the band gap. The reciprocal QVH insulator $(0, \pm\beta_{\mathrm{I}})$ supports bidirectional propagation features, whereas the valley-Chern insulator $(\alpha_{\mathrm{IV}}, -\beta_{\mathrm{I}})$ results in a phase II one-way system. We emphasize that there are two gapless localized states along the QH-QH interface, but only one for the QH-QVH case, matching the prediction of the bulk-edge correspondence. Figure 4(g) illustrates the extent of the three kinds of lattice-scale defects introduced: (1) bends with sharp corners, (2) a cavity created by removing some resonators, and (3) local disorder perturbed by varying $R_{\mathrm{out}}^{\pm}$ in a normal distribution ($\sigma = 0.1R_{\mathrm{out}}$). At the input side, we place two monopole sources (green dots) and sweep their frequency to predict the outgoing energy flux, E_{out}. All spectra that are plotted in Figs. 4(d)–4(f) display a small descent of E_{out} against the frequency within the gap. Other than this, what clearly stands out is the entirely unaffected outgoing energy flux of in-gap edge states for the Chern-insulator (QH-QH) when the three defect scenarios are added. Maintaining the same geometrical setting, but reverting to the entirely reciprocal valley-Hall system (QVH-QVH), the E_{out} spectrum unequivocally displays strongly deteriorating characteristics to the said lattice-scale imperfections in the form of strong flux reductions and oscillations as seen in Fig. 4(e). In the last example the interface states confine along the separation between a Chern and a valley insulator (QH-QVH) which is tuned at the critical phase II [see Fig. 1(b)]. As we mentioned, this valley-Chern insulator remains nonreciprocal despite containing a valley-based insulator. Still, as Fig. 4(f) renders, within the band gap, despite the numbers of intentionally added imperfections, the spectrum remarkably displays great similarity to the pure Chern insulator as presented in Fig. 4(d). This surprising effect means that we are permitted to relax the necessary number of TS breaking resonators, in that they may reside only within a single insulator-half, still being able to sustain highly topologically robust one-way edge states within this valley-Chern insulator. Corresponding computed intensity maps as shown in Figs. 4(g)–4(i) corroborate our conclusions that insulators with fully or partially introduced TS breaking units surpass a valley-Hall insulator in terms of the resilience against typically wave-based obstacles and defects. As was discussed elsewhere [25], lattice-scale defects have a severe influence on valley-Hall interface states thanks to unavoidable intervalley scattering. In the Supplemental Material we provide additional simulations to corroborate our claims [36].

In conclusion, we have demonstrated an acoustic valley-polarized one-way Dirac spectrum resulting from competing effects of Chern and valley physics in man-made lattices. Surprisingly, such valley-Chern insulators sustain topological nonreciprocal band inversion that is controlled by the in-resonator flow. Simultaneously, at the opposite valley, the same TS breaking mechanism is widening the gap, thus increasing the bandwidth of valley-polarized one-way edge states. Further, a deliberate comparative study displays how a valley-Chern insulator can compete with a conventional Chern insulator in that they both do not yield to lattice-scale crystal obstacles and imperfections as opposed to the much more defect-susceptible valley-Hall insulator. We foresee that our work may inspire novel avenues for topologically robust and nonreciprocal sound guiding.

J.C. acknowledges support from the European Research Council (ERC) through the Starting Grant No. 714577 PHONOMETA and from the MINECO through a Ramón y Cajal grant (Grant No. RYC-2015-17156). Z.Z. acknowledges support from the China Scholarship Council.

[1] X.-L. Qi and S.-C. Zhang, Rev. Mod. Phys. **83**, 1057 (2011).

[2] T. Ozawa, H. M. Price, A. Amo, N. Goldman, M. Hafezi, L. Lu, M. C. Rechtsman, D. Schuster, J. Simon, O. Zilberberg *et al.*, Rev. Mod. Phys. **91**, 015006 (2019).

[3] X. Zhang, M. Xiao, Y. Cheng, M.-H. Lu, and J. Christensen, Commun. Phys. **1**, 97 (2018).

[4] F. D. M. Haldane and S. Raghu, Phys. Rev. Lett. **100**, 013904 (2008).

[5] Z. Wang, Y. Chong, J. D. Joannopoulos, and M. Soljačić, Nature (London) **461**, 772 (2009).

[6] Z. Yang, F. Gao, X. Shi, X. Lin, Z. Gao, Y. Chong, and B. Zhang, Phys. Rev. Lett. **114**, 114301 (2015).

[7] A. B. Khanikaev, R. Fleury, S. H. Mousavi, and A. Alu, Nat. Commun. **6**, 8260 (2015).

[8] X. Ni, C. He, X.-C. Sun, X.-p. Liu, M.-H. Lu, L. Feng, and Y.-F. Chen, New J. Phys. **17**, 053016 (2015).

[9] Z.-G. Chen and Y. Wu, Phys. Rev. Appl. **5**, 054021 (2016).

[10] L. M. Nash, D. Kleckner, A. Read, V. Vitelli, A. M. Turner, and W. T. Irvine, Proc. Natl. Acad. Sci. USA **112**, 14495 (2015).

[11] P. Wang, L. Lu, and K. Bertoldi, Phys. Rev. Lett. **115**, 104302 (2015).

[12] A. B. Khanikaev, S. H. Mousavi, W.-K. Tse, M. Kargarian, A. H. MacDonald, and G. Shvets, Nat. Mater. **12**, 233 (2013).

[13] M. Hafezi, S. Mittal, J. Fan, A. Migdall, and J. Taylor, Nat. Photonics **7**, 1001 (2013).

[14] L.-H. Wu and X. Hu, Phys. Rev. Lett. **114**, 223901 (2015).
[15] C. He, X. Ni, H. Ge, X.-C. Sun, Y.-B. Chen, M.-H. Lu, X.-P. Liu, and Y.-F. Chen, Nat. Phys. **12**, 1124 (2016).
[16] Z. Zhang, Q. Wei, Y. Cheng, T. Zhang, D. Wu, and X. Liu, Phys. Rev. Lett. **118**, 084303 (2017).
[17] Y. Deng, H. Ge, Y. Tian, M. Lu, and Y. Jing, Phys. Rev. B **96**, 184305 (2017).
[18] R. Süsstrunk and S. D. Huber, Science **349**, 47 (2015).
[19] M. Miniaci, R. K. Pal, B. Morvan, and M. Ruzzene, Phys. Rev. X **8**, 031074 (2018).
[20] S.-Y. Yu, C. He, Z. Wang, F.-K. Liu, X.-C. Sun, Z. Li, H.-Z. Lu, M.-H. Lu, X.-P. Liu, and Y.-F. Chen, Nat. Commun. **9**, 3072 (2018).
[21] J. Noh, S. Huang, K. P. Chen, and M. C. Rechtsman, Phys. Rev. Lett. **120**, 063902 (2018).
[22] F. Gao, H. Xue, Z. Yang, K. Lai, Y. Yu, X. Lin, Y. Chong, G. Shvets, and B. Zhang, Nat. Phys. **14**, 140 (2018).
[23] J. Lu, C. Qiu, L. Ye, X. Fan, M. Ke, F. Zhang, and Z. Liu, Nat. Phys. **13**, 369 (2017).
[24] J. Lu, C. Qiu, W. Deng, X. Huang, F. Li, F. Zhang, S. Chen, and Z. Liu, Phys. Rev. Lett. **120**, 116802 (2018).
[25] Z. Zhang, Y. Tian, Y. Cheng, Q. Wei, X. Liu, and J. Christensen, Phys. Rev. Appl. **9**, 034032 (2018).
[26] Z. Zhang, Y. Tian, Y. Wang, S. Gao, Y. Cheng, X. Liu, and J. Christensen, Adv. Mater. **30**, 1803229 (2018).
[27] X. Han, Y.-G. Peng, L. Li, Y. Hu, C. Mei, D.-G. Zhao, X.-F. Zhu, and X. Wang, Phys. Rev. Appl. **12**, 014046 (2019).
[28] M. Yan, J. Lu, F. Li, W. Deng, X. Huang, J. Ma, and Z. Liu, Nat. Mater. **17**, 993 (2018).
[29] M. Miniaci, R. K. Pal, R. Manna, and M. Ruzzene, Phys. Rev. B **100**, 024304 (2019).
[30] P. Gao, D. Torrent, F. Cervera, P. San-Jose, J. Sánchez-Dehesa, and J. Christensen, Phys. Rev. Lett. **123**, 196601 (2019).
[31] C.-W. Chen, N. Lera, R. Chaunsali, D. Torrent, J. V. Alvarez, J. Yang, P. San-Jose, and J. Christensen, Adv. Mater. **31**, 1904386 (2019).
[32] Y. Ding, Y. Peng, Y. Zhu, X. Fan, J. Yang, B. Liang, X. Zhu, X. Wan, and J. Cheng, Phys. Rev. Lett. **122**, 014302 (2019).
[33] J. Lu, C. Qiu, S. Xu, Y. Ye, M. Ke, and Z. Liu, Phys. Rev. B **89**, 134302 (2014).
[34] F. D. M. Haldane, Phys. Rev. Lett. **61**, 2015 (1988).
[35] S. Raghu and F. D. M. Haldane, Phys. Rev. A **78**, 033834 (2008).
[36] See Supplemental Material at http://link.aps.org/supplemental/10.1103/PhysRevB.101.020301 for the effect of lattice scale defects on topological waveguiding.